# *Chirality-Dependent Second Harmonic Generation of MoS 2 Nanoscroll with Enhanced Efficiency*



**Citation:** Qingkai Qian, Rui Zu, Qingqing Ji, Gang Seob Jung, Kunyan Zhang, Ye Zhang, Markus J. Buehler, Jing Kong, Venkatraman Gopalan, and Shengxi Huang, Chirality-Dependent Second Harmonic Generation of MoS2 Nanoscroll with Enhanced Efficiency, ACS Nano 2020 14 (10)

**As Published:** 10.1021/ACSNANO.0C05189

**Publisher:** American Chemical Society (ACS)

**Persistent URL:** https://hdl.handle.net/1721.1/132719

**Version:** Author's final manuscript: final author's manuscript post peer review, without publisher's formatting or copy editing

# Chirality-Dependent Second Harmonic Generation of $MoS_2$ Nanoscroll with Enhanced Efficiency

*Qingkai Qian,[†] Rui Zu,[‡] Qingqing Ji,[#] Gang Seob Jung,[∥,⊥] Kunyan Zhang,[†] Ye Zhang,[#,§] Markus J. Buehler,[⊥] Jing Kong,[#] Venkatraman Gopalan,[‡] Shengxi Huang*[,†]*

[†]Department of Electrical Engineering, The Pennsylvania State University, University Park, Pennsylvania 16802, United States

[‡]Department of Materials Science and Engineering, The Pennsylvania State University, University Park, Pennsylvania 16802, United States

[#]Department of Electrical Engineering, Massachusetts Institute of Technology, Cambridge, Massachusetts 02139, United States

[∥]Computational Sciences and Engineering Division, Oak Ridge National Laboratory, Oak Ridge, Tennessee 37831, United States

[⊥]Department of Civil and Environmental Engineering, Massachusetts Institute of Technology, Cambridge, Massachusetts 02139, United States

[§]Department of Physics, Mount Holyoke College, South Hadley, Massachusetts 01075, United States

KEYWORDS: $MoS_2$, nanoscroll, nanotube, second harmonic generation, chirality.

## ABSTRACT

Materials with high second harmonic generation (SHG) efficiency and reduced dimensions are favorable for integrated photonics and novel nonlinear optical applications. Here, we fabricate $MoS_2$ nanoscrolls with different chiralities and study their SHG performances. As a 1D material, $MoS_2$ nanoscroll shows reduced symmetry and strong chirality dependency in the polarization-resolved SHG characterizations. This SHG performance can be well explained by the coherent superposition theory of second harmonic field of the nanoscroll walls. $MoS_2$ nanoscrolls with certain chiralities in our experiment can have SHG intensity up to 98 times stronger than that of monolayer $MoS_2$, and the full potential can still be further exploited. The same chirality-dependent SHG can be expected for nanoscrolls or nanotubes composed of other non-centrosymmetric 2D materials, such as $WS_2$, $WSe_2$, and hBN. The characterization and analysis results presented here can also serve as a non-destructive technique to determine the chiralities of these nanoscrolls and nanotubes.

## INTRODUCTION

The development of nonlinear optics largely relies on emerging material systems that possess high nonlinear susceptibility, processability, and ease of photonic integration and device miniaturization, which has been actively pursued for decades among the optics community.[1-8] Second harmonic generation (SHG), as an essential nonlinear optical effect, is broadly used for applications such as frequency conversion, light modulation, and material characterizations.[9-15] Yet, the required noncentrosymmetry of the host crystals greatly limits the search for SHG-

bearing materials.[2,6,8,11,16] One recent advance that mitigates this is the rise of two-dimensional materials, such as monolayer transition metal dichalcogenides (TMDs), which generally have reduced crystal symmetries than their bulk counterparts and exhibit strong SHG signals considering their atomic thicknesses.[3,4,11,17] The atomic scale can also enable miniature device fabrication and integration. Nevertheless, the ultimately scaled thickness of such 2D materials poses a great challenge in their insufficient light-matter interaction. While naturally-existing bulk TMDs are in the Bernal-stacking 2H phase with restored centrosymmetry and thus vanished SHG,[6-8] and the synthesized 3R phase still faces the problems of synthesis difficulty and phase instability,[18] a method capable of aligning the constituent layers in the multilayer/bulk TMDs without symmetry restoration is highly desired to realize phase-matched SHG signal of each layer for constructive interference and enhancement of the SHG intensity up to a practically functional level.

One-dimensional nanomaterials such as multi-walled nanotubes and nanoscrolls, as a nanostructure derivative of 2D materials with further reduced symmetry, represent a promising platform to engineer the interlayer interaction for novel optical and optoelectronic properties.[19-26] In particular, the nanoscroll structure of a TMD monolayer with a specific chirality, which is defined as the rolling angle, can be fabricated and identified with a simple solvent-evaporation-driven processes,[21,23,25] which is capable of controlling the inherent alignment of the constituent layers, a long-pursued structural property for SHG enhancement. Moreover, the reduced dimensionality could give rise to anisotropy in the nonlinear optical response that holds promise for miniaturized polarization-dependent applications. These aspects, however, are still experimentally underexplored.

In this work, we fabricate 1D $MoS_2$ nanoscrolls out of chemical vapor deposition (CVD) $MoS_2$ monolayers, using a solvent-evaporation-driven rolling process.[21,23,25] We determine the nanoscroll chiralities (*i.e.*, rolling directions) from the unscrolled triangular monolayer parts and reveal an anisotropic and chirality-dependent SHG enhancement up to two orders of magnitude compared with monolayer $MoS_2$. A model by considering coherent second harmonic (SH) field superposition is established and well explains the SHG properties of the $MoS_2$ nanoscrolls. The work presented here could enable a new paradigm in constructing and designing miniaturized anisotropic nonlinear optical nanostructures from noncentrosymmetric 2D materials.

## RESULTS AND DISCUSSION

$MoS_2$ nanoscrolls are directly obtained by rolling $MoS_2$ flakes through a solvent-evaporation-driven process.[21,23,25] The triangular $MoS_2$ flakes are grown on $SiO_2$/Si substrate by CVD, with $MoO_3$ and sulfur powders as the solid precursors. By dropping isopropyl alcohol (IPA) solution on the surface, the vaporization of IPA causes $MoS_2$ flakes to roll into quasi-1D nanoscrolls at room temperature within several minutes. Figure 1a shows a partially scrolled $MoS_2$ flake that is typically obtained. Based on the 60° vertex angle and the sharpness of the triangle edges, this $MoS_2$ flake can be determined to be Mo-zigzag edge terminated,[27] and the atomic structure is schematically drawn over the flake in Figure 1a.

Polarization-resolved SHG is first measured in the planar area (Red dot in Figure 1a). The sample is excited by a Ti: Sapphire femtosecond laser system (80 fs, 80 MHz, chopped at 1 kHz) centered at 800 nm, through a 50× objective (NA = 0.75). The polarization of incident laser is

continuously tuned by a motorized half-wave plate. The resulting SHG signal is collected by the same objective and selected by a dichroic mirror. In previous polarization-resolved SHG measurements, the SHG signals of TMDs are usually measured with the analyzer polarized parallel or perpendicular to the polarization of incident laser by rotating the sample, which leads to six-fold petals in the polarization-resolved SHG pattern.[4,6,8,11,13,14] However, in our experiment, considering the relative small diameter of the quasi-1D nanoscroll, the change of laser beam position during rotating the sample may lead to a large variation of SHG intensity. Therefore, for accuracy and consistency, in all of our polarization-resolved SHG measurements, the SHG signals are collected by fixing the linear analyzer along *x* or *y* direction, while rotating the polarization of the incident laser. The *x*- and *y*-polarized measurements result in four-fold petals (Figure 1b), which is consistent with our numerical analysis (See Supporting Information Section 1). After fitting the results by the solid lines in Figure 1b, polarization-resolved SHG of monolayer $MoS_2$ analyzed with parallel and perpendicular polarizations with respect to the incident laser can be converted (See Supporting Information Section 1) and is shown in Figure 1c. The petal orientations agree with the atomic configuration in Figure 1a.

To investigate the SHG intensity of the $MoS_2$ nanoscrolls, we measured the SHG for the square region (green dashed line) in Figure 1a by scanning the sample using a piezo-driven sample stage. The SHG signal is detected by fixing the linear analyzer along *x* direction, while the incident laser is polarized along 36° as indicated by the blue arrow in Figure 1b. This laser polarization makes the monolayer $MoS_2$ reach its maximum SHG intensity in this analyzing configuration. The mapping results are shown in Figure 1d, with the polarizations of incident laser and analyzer also shown as the inset. A homogenous SHG intensity is observed for the flat region of $MoS_2$ flake, while the nanoscrolls, such as the ones noted by *NS1* and *NS2* in Figure 1d,

show remarkably higher SHG intensities, which are 14 and 5.2 times larger than that of monolayer $MoS_2$ in this measurement configuration.

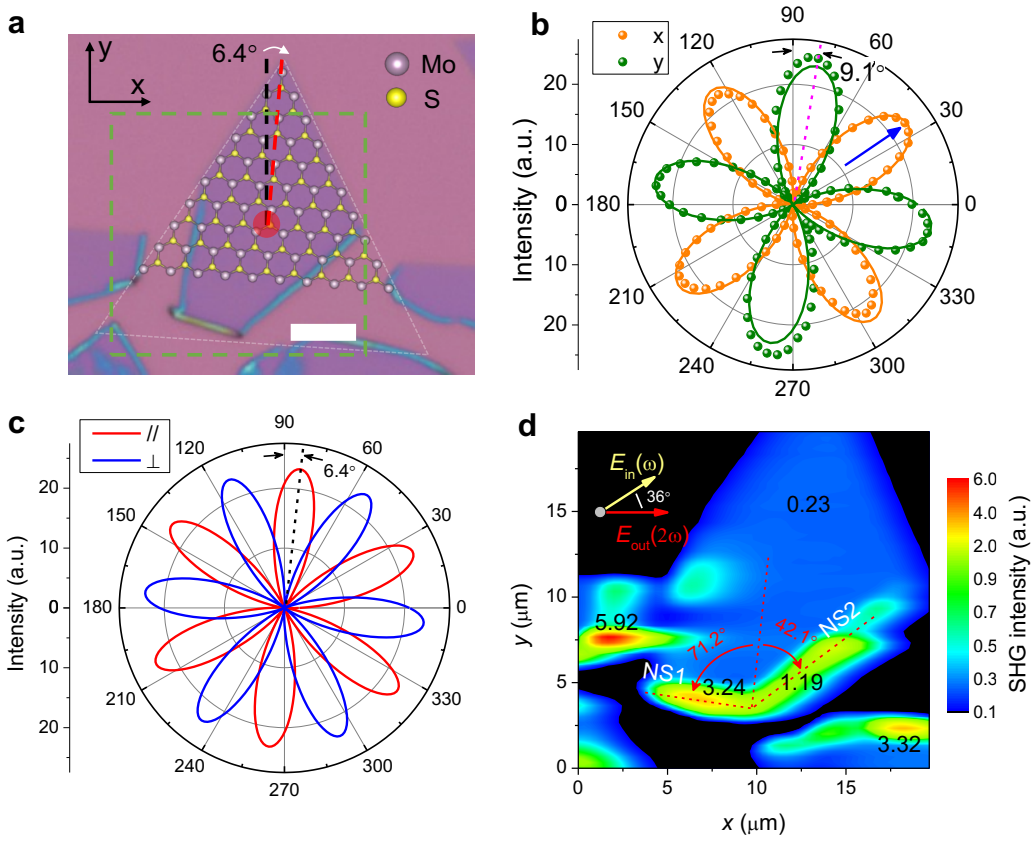


**Figure 1.** (a) Optical image of CVD-grown single-layer $MoS_2$ film and the formed nanoscrolls. Scale bar: 5 μm. (b) Polarization-resolved second harmonic generation (SHG) of $MoS_2$ monolayer measured at the red dot position in (a) with the second harmonic (SH) polarized along *x* and *y* directions. The dots are experimental results, while the solid lines are theoretical fittings. (c) Converted polarization-resolved SHG of $MoS_2$ film with SH polarized along parallel and perpendicular directions with respect to the incident laser polarization. (d) SHG intensity mapping of $MoS_2$ monolayer and the nanoscrolls in the green dashed square region of (a). The incident laser

during the mapping is polarized along direction indicated by the blue arrow in (b), while the SHG signal is analyzed along *x* direction.

Figure 2a schematically shows the rolling of the nanoscroll. The rolling direction of nanoscroll $\theta_{\mathrm{roll}}$ is defined as the angle between the nanoscroll axis and the Mo-S bond direction of the triangular flake (*i.e.* armchair direction). The enhanced SHG from the nanoscrolls is owing to the coherent superposition of the SH fields from the constituent monolayer walls, which accumulate differently depending on the rolling direction, *i.e.*, the chirality of the nanoscrolls. Before touching upon this, we first consider the SHG of planar $MoS_2$ monolayer, whose SH field can be calculated from the second-order susceptibility tensor under the constraints of a $P\bar{6}m2$ space group,[7,16,17]

$$\chi_{ijk}^{(2)} = d_0 \begin{pmatrix} \begin{pmatrix} 0 \\ -1 \\ 0 \end{pmatrix} & \begin{pmatrix} -1 \\ 0 \\ 0 \end{pmatrix} & \begin{pmatrix} 0 \\ 0 \\ 0 \end{pmatrix} \\ \begin{pmatrix} -1 \\ 0 \\ 0 \end{pmatrix} & \begin{pmatrix} 0 \\ 1 \\ 0 \end{pmatrix} & \begin{pmatrix} 0 \\ 0 \\ 0 \end{pmatrix} \\ \begin{pmatrix} 0 \\ 0 \\ 0 \end{pmatrix} & \begin{pmatrix} 0 \\ 0 \\ 0 \end{pmatrix} & \begin{pmatrix} 0 \\ 0 \\ 0 \end{pmatrix} \end{pmatrix} \qquad (1)$$

Here $\chi_{ijk}^{(2)}$ is a third-order tensor, *i, j, k* are indexes that can be *x*, *y* or *z* axis, $d_0$ is a constant related to the susceptibility amplitude of monolayer $MoS_2$. The large parenthesis in equation 1 is for *i, j* indexes, while the smaller inner parenthesis means the change of *k* index. To get eq 1, the armchair direction (*i.e.*, the direction of Mo-S bonds) of triangular $MoS_2$ flake is aligned with *y* axis. Using this tensor, the SH field $E_i^{2\omega}$ (or proportionally the generated SH electric dipole) can be calculated by $E_i^{2\omega} = \chi_{ijk}^{(2)} E_j^{\omega} E_k^{\omega}$, in which $E_j^{\omega}$ and $E_k^{\omega}$ is the axial components of incident laser electric field. Here the Einstein summation notation is used. For different excitation

polarizations, the SH field of a monolayer $MoS_2$ calculated using eq 1 is schematically drawn in Figure 2b. Specifically, for excitation polarized along the armchair direction of the $MoS_2$ flake, the SH field is along the same direction, while for excitation perpendicular to the armchair direction, that is, along the zigzag direction, the induced SH field is perpendicular to incident polarization. We note that because the SH field $E_i^{2\omega}$ depends on the incident electric field $E_j^{\omega}$ through $E_i^{2\omega} = \chi_{ijk}^{(2)} E_j^{\omega} E_k^{\omega}$, it maintains the same direction for both positive and negative $E_j^{\omega}$.

The second-order susceptibility tensor $\chi_{ijk}^{(2)}$ of $MoS_2$ flake changes its mathematical form after rotation to become a part of nanoscroll walls. The mathmetical transformation is provided below in eq 2.

$$\chi_{ijk}^{(2)}(R) = R_{im}\, \chi_{mnp}^{(2)}\, {R^{-1}}_{nj}\, {R^{-1}}_{pk} \qquad (2)$$

Here $R$ is the rotation matrix with matrix elements $R_{ij}$, and $R^{-1}$ is the inverse matrix of $R$. The detailed derivation can be found in Supporting Information Section 2. Based on the rotated tensor, SH fields contributed by nanoscroll walls can be calculated. Figure 2c illustrates the SH field distributions of a nanoscroll with $\theta_{\text{roll}} = 0°$, under excitation laser polarized parallel and perpendicular to the nanoscroll axis respectively. For incident laser parallel to the nanoscroll axis, the rolling of the $MoS_2$ flake does not change the orientation of the incident field relative to the $MoS_2$ lattice. As a result, the generated SH fields from different parts of the whole nanoscroll are still in the same direction, and the total SH dipole is the simple summation of the contributions without phase losses, which greatly enhances the SHG efficiency. For incident laser polarized perpendicular to nanoscroll axis, a slightly different SHG will be found, because the rolling of the $MoS_2$ flake now changes the direction of the incident laser polarization relative

to the rolled $MoS_2$ lattice. For example, the electric field of the incident laser changes its sign relatively to the top and bottom parts of the nanoscroll. As mentioned above, the SH field maintains the same direction regardless of a positive or negative incident electric field. Therefore, the SH fields are still in-phase for enhanced emission. Nevertheless, because the incident electric field is out-of-plane for the vertical sidewalls of the nanoscroll, the overall SHG response is weaker than the incident polarization along the nanoscroll axis.

The SHG intensity can be enhanced for nanoscrolls, but the rolling direction (*i.e.* chirality) of the nanoscrolls will greatly influence the SHG efficiency. Figure 2d shows the SH field superposition for a nanoscroll rolled along the zigzag direction ($\theta_{\mathrm{roll}} = 30°$). No matter whether the excitation polarization is parallel or perpendicular to the nanoscroll axis, the SH field is always perpendicular to the nanoscroll axis, and the SH dipole is always oriented spirally around the nanoscroll axis as indicated by the red arrows. Consequently, the total SH field will cancel each other, leading to a weak SHG intensity.

To quantitatively evaluate the chirality-dependent SHG emission of $MoS_2$ nanoscrolls, as an approximation, we calculate the effective second-order susceptibility tensor of a single-walled $MoS_2$ nanotube. This approximation ignores the continuous increase of the nanoscroll diameter, but it captures the essence of the rolled $MoS_2$ flake. Based on the coherent superposition theory, the effective second-order susceptibility tensor of the single-walled nanoscroll/nanotube can be calculated by summing the susceptibility tensor of the constituent walls together,

$$\chi_{ijk}^{(2)}(\text{nanoscroll}) = \int_0^{2\pi} \chi_{ijk}^{(2)}\left(R_{\varphi,\theta_{roll},\varphi_{roll}}\right) d\varphi_{roll}/2\pi \quad (3)$$

in which $R_{\varphi,\theta_{roll},\varphi_{roll}}$ is the rotation matrix of $MoS_2$ flake from the planar orientation to a part of the nanoscroll/nanotube walls, $\varphi$ is the rotation angle of the triangular flake from the *y* axis (*e.g.* $\varphi = -6.4°$ in Figure 1a), $\theta_{roll}$ is the chirality of the nanoscroll/nanotube as defined in Figure 2a, $\varphi_{roll}$ is the rolling angle around the nanoscroll axis, which varies from 0 to $2\pi$, then $\chi^{(2)}_{ijk}\left(R_{\varphi,\theta_{roll},\varphi_{roll}}\right)$ is the second-order susceptibility tensor of $MoS_2$ monolayer after rotation by $R_{\varphi,\theta_{roll},\varphi_{roll}}$ according to eq 2. This second-order susceptibility tensor of nanoscroll is normalized by its total composed $MoS_2$ monolayer area.

The polarization revolved SHG emission patterns of $MoS_2$ nanoscrolls with different chiralities are calculated and presented in Figure 2e based on eq 3. Similar to monolayer $MoS_2$, the polarization-resolved parallel and perpendicular SHG signals of nanoscrolls have six petals. Consistent with the qualitative analyses of Figure 2c and 2d, a nanoscroll with $\theta_{roll} = 0°$ has the largest SHG intensity, while nanoscroll with $\theta_{roll} = 30°$ has zero SHG intensity. Because of the three-fold rotation symmetry of monolayer $MoS_2$ and the $\pi$ rotation equivalence of SHG measurement, the SHG pattern of nanoscroll with $\theta_{roll} = 60°$ has restored to the same SHG pattern as that of $\theta_{roll} = 0°$, only with a $60°$ rotation for the entire polarization-resolved SHG patterns.

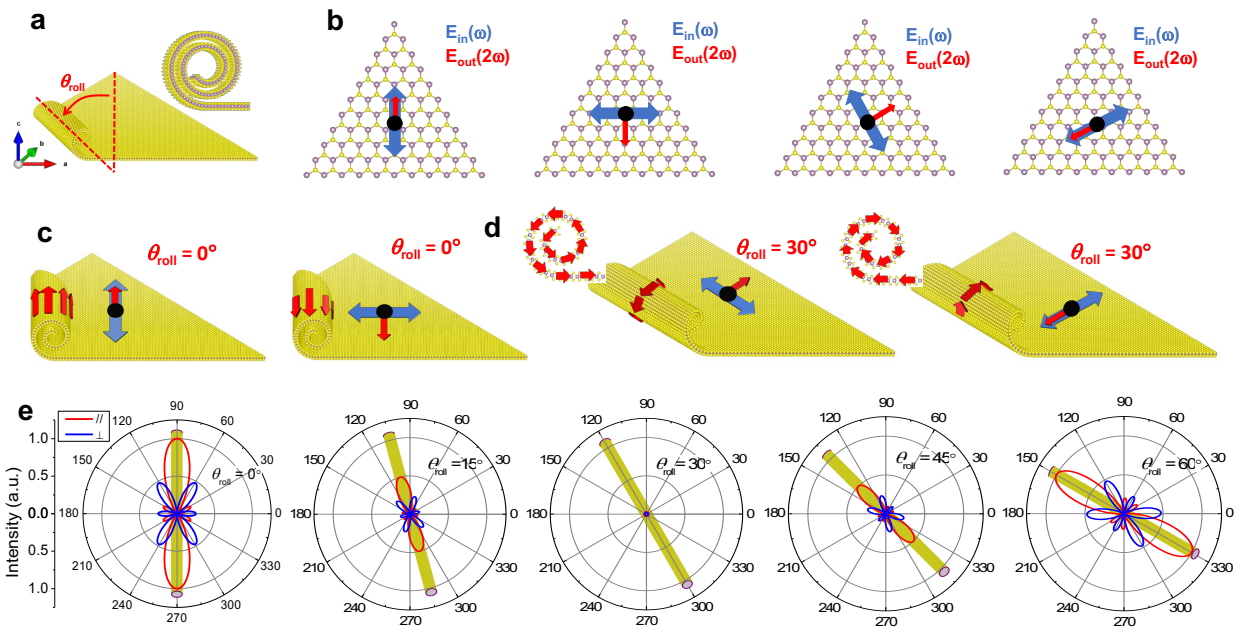


**Figure 2.** (a) Schematic of $MoS_2$ nanoscroll. (b) Electric fields (or dipoles) of the second harmonic induced by different incident laser polarizations. Schematics of second harmonic electric fields (dipoles) in a nanoscroll with (c) $\theta_{roll} = 0°$ and (d) $\theta_{roll} = 30°$ induced by incident laser polarized along and perpendicular to the nanoscroll axis respectively. (e) Calculated polarization-resolved SHG of $MoS_2$ nanoscrolls with different chiralities.

We note that the highest SHG intensities of $MoS_2$ nanoscrolls in Figure 2e are always achieved when the laser excitation and the analyzer are both polarized along the nanoscroll axis. This can also be understood from the susceptibility tensor of nanoscroll. Based on eq 3, the SH susceptibility tensor for a nanoscroll can be calculated to be,

$$\chi^{(2)}_{ijk}(\text{nanoscroll}) = d_0 \cos 3\theta_{roll} \begin{pmatrix} \begin{pmatrix} 0 \\ -0.5 \\ 0 \end{pmatrix} & \begin{pmatrix} -0.5 \\ 0 \\ 0 \end{pmatrix} & \begin{pmatrix} 0 \\ 0 \\ 0 \end{pmatrix} \\ \begin{pmatrix} -0.5 \\ 0 \\ 0 \end{pmatrix} & \begin{pmatrix} 0 \\ 1 \\ 0 \end{pmatrix} & \begin{pmatrix} 0 \\ 0 \\ -0.5 \end{pmatrix} \\ \begin{pmatrix} 0 \\ 0 \\ 0 \end{pmatrix} & \begin{pmatrix} 0 \\ 0 \\ -0.5 \end{pmatrix} & \begin{pmatrix} 0 \\ -0.5 \\ 0 \end{pmatrix} \end{pmatrix} \quad (4)$$

in which $\theta_{roll}$ is the roll direction defined in Figure 2a. We note that to simplify the matrix form of this tensor, the axis of the nanoscroll is selected to be *y* axis here (See Supporting Information Section 3 for tensor form after rotation). From eq 4, it can be clearly seen that the highest SHG intensity is caused by $\chi^{(2)}_{yyy} = d_0 \cos 3\theta_{roll}$. In contrast to the tensor of monolayer $MoS_2$ in eq 1, the nonzero elements of this nanoscroll tensor in the *x*-*y* plane are related by $\chi^{(2)}_{xxy} = \chi^{(2)}_{xyx} = \chi^{(2)}_{yxx} = -\chi^{(2)}_{yyy}/2$, instead of $\chi^{(2)}_{xxy} = \chi^{(2)}_{xyx} = \chi^{(2)}_{yxx} = -\chi^{(2)}_{yyy}$ for planar monolayer $MoS_2$. The smaller ratio of $\chi^{(2)}_{xxy}$, $\chi^{(2)}_{xyx}$ and $\chi^{(2)}_{yxx}$ with respect to $\chi^{(2)}_{yyy}$ in the nanoscroll is caused by the out-of-plane electric field for the vertical nanoscroll sidewalls as mentioned in Figure 2c, which makes the effective exciting electric field smaller.

For the above calculation, we have assumed that the cross-section of nanoscroll is circular. However, because of the substrate influence or the rolling dynamics, the cross-section of nanoscroll can be elliptical (see Supporting Information Section 4),[23,28] which will change the sidewall contributions to the SHG intensity. The ellipticity can be defined by $e = (a - b)/(a + b)$, in which *a* and *b* are axes indicated in Figure 3a. For nanoscroll with elliptical cross-section, there is no accurate analytical form for the second-order susceptibility tensor, but the tensor can be numerically calculated and well approximated by the analytical eq 5. All the tensor element elements have approximation errors smaller than 0.014 (See Supporting Information Section 5), which are ignorable compared with the largest element 1 in the parentheses.

$$\chi^{(2)}_{ijk}(\text{elliptical nanoscroll}) \approx d_0 \cos 3\theta_{roll} \begin{pmatrix} \begin{pmatrix} 0 \\ -0.5 - 0.5\sin\left(\frac{e\pi}{2}\right) \\ 0 \end{pmatrix} & \begin{pmatrix} -0.5 - 0.5\sin\left(\frac{e\pi}{2}\right) \\ 0 \\ 0 \end{pmatrix} & \begin{pmatrix} 0 \\ 0 \\ 0 \end{pmatrix} \\ \begin{pmatrix} -0.5 - 0.5\sin\left(\frac{e\pi}{2}\right) \\ 0 \\ 0 \end{pmatrix} & \begin{pmatrix} 0 \\ 1 \\ 0 \end{pmatrix} & \begin{pmatrix} 0 \\ 0 \\ -0.5 + 0.5\sin\left(\frac{e\pi}{2}\right) \end{pmatrix} \\ \begin{pmatrix} 0 \\ 0 \\ 0 \end{pmatrix} & \begin{pmatrix} 0 \\ 0 \\ -0.5 + 0.5\sin\left(\frac{e\pi}{2}\right) \end{pmatrix} & \begin{pmatrix} 0 \\ -0.5 + 0.5\sin\left(\frac{e\pi}{2}\right) \\ 0 \end{pmatrix} \end{pmatrix} \quad (5)$$

Figure 3 numerically calculates the polarization-resolved SHG patterns of nanoscrolls/nanotubes with an elliptical cross-section. All these nanoscrolls are rolled with $\theta_{roll} = 0°$ and have the same perimeter. For nanoscroll with oblate cross-section ($e = 0.3$ in Figure 3a), because its sidewall has less contribution, the SHG intensity is stronger than those with circular ($e = 0$) and prolate ($e < 0$) cross-sections, when the incident laser is not polarized along the nanoscroll axis. This trend can be more easily understood from eq 5 by the extreme case when $e = 1$ or $e = -1$, which just becomes a tensor of horizontally or vertically oriented $MoS_2$ bilayers. This numerical analysis also further validates our previous vertical sidewall explanation of the decreased ratio between $\chi^{(2)}_{xxy}$, $\chi^{(2)}_{xyx}$, $\chi^{(2)}_{yxx}$ and $\chi^{(2)}_{yyy}$ for nanoscrolls.

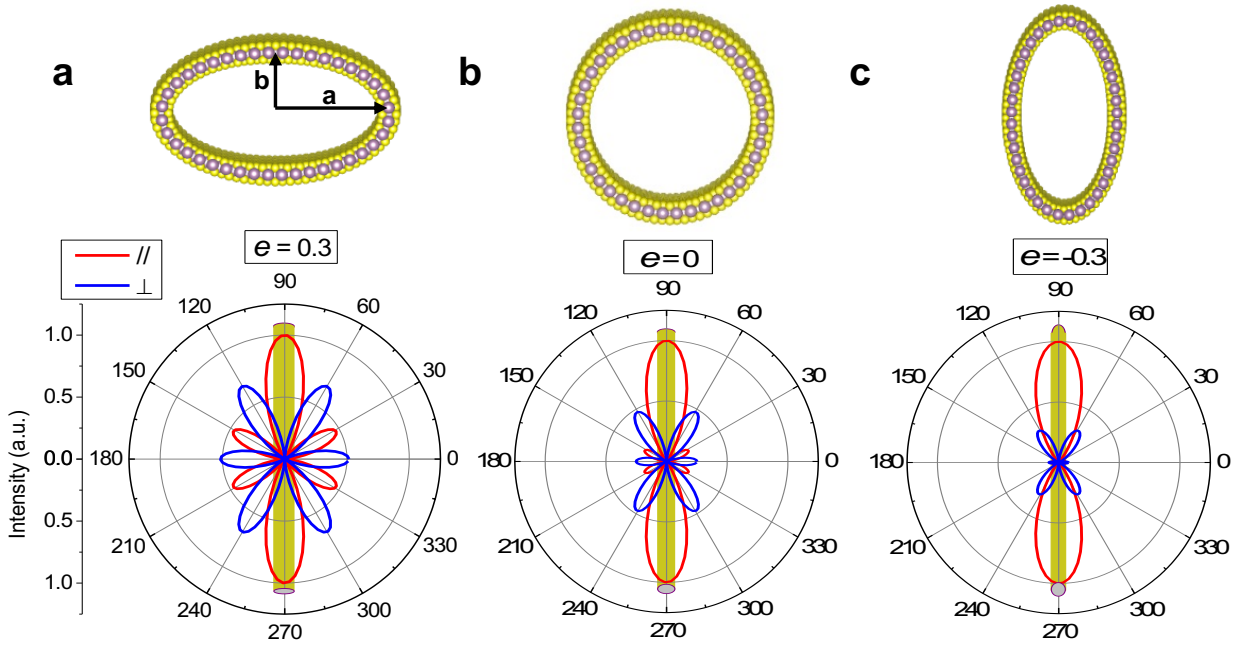


**Figure 3.** (a-c) Calculated polarization resolved SHG of $MoS_2$ nanoscrolls/nanotubes with different elliptical cross-sections. The nanoscrolls/nanotubes are rolled with $\theta_{roll} = 0°$. Ellipticity of the cross-section is defined by $e = (a - b)/(a + b)$. Nanotube with positive ellipticity in (a)

has large side petals compared with nanotubes in (b) and (c), due to its smaller area of vertical sidewalls.

Figure 4a and 4b show the experimentally measured polarization-resolved SHG of two nanoscrolls (*NS1* and *NS2* in Figure 1d), with SHG electric field analyzed along *x* and *y* directions. The SHG patterns also show four petals, similar to the case of planar $MoS_2$ monolayer in Figure 1b. However, the absolute intensities of the four SHG petals are much larger than that of monolayer $MoS_2$. Besides, the intensities of the four petals are not equal, indicating a symmetry breaking caused by $MoS_2$ scrolling. Using the parameters of $MoS_2$ flake rotation angle ($\varphi = -6.4°$ in Figure 1a) and the scroll direction $\theta_{roll}$ of the two nanoscrolls (71.2° and –42.1° in Figure 1d), the second-order susceptibility tensors are calculated according to eq 3, based on which the polarization-resolved SHG patterns are calculated and plotted in Figure 4c and 4d (solid lines). During the calculations, we have used the second-order susceptibility tensor of single-walled nanoscroll/nanotube, since the further scrolling only linearly increases the tensor magnitude. The only fitting parameter is the scaling factor of SHG intensity, which is influenced by the detection sensitivities and equipment settings.

The theoretical calculations show excellent agreement with the experimental results, in terms of both polarization dependencies and relative intensities, which validates the coherent superposition analyses of SH field above. There are still some intensity discrepancies for the relatively weak petals of both nanoscrolls. By considering the possible elliptical cross-section of nanoscrolls due to substrate interaction or the scrolling dynamics, SHG pattern of nanoscroll *NS1* with ellipticity $e = 0.15$ is calculated and plotted as the dashed lines in Figure 4c, which shows an improved agreement with the experimental intensities regarding the weak petals. However,

the discrepancies for nanoscroll *NS2* are significantly different, especially for the *x*-polarized SHG pattern, which has no mirror symmetry. Based on the second-order susceptibility tensor $\chi$, the *x*-polarized SHG intensity is proportional to $(\frac{\chi_{xxx}+\chi_{xyy}}{2} + \chi_{xxy} \cdot sin2\theta + \frac{\chi_{xxx}-\chi_{xyy}}{2} \cdot cos2\theta)^2$, which will always have mirror symmetry (See Supporting Information Section 6). As a result, the SHG pattern deviations for nanoscroll *NS2* cannot be explained by a simple second-order susceptibility tensor and might need to consider the wave propagation effect.[11,29]

The SHG patterns detected with parallel and perpendicular polarization settings for these two nanoscrolls are converted in Figure 4e and 4f, based on the fittings above. According to Figure 4e and 4f, the highest SHG intensities are obtained when both the incident laser and the detection polarizer are polarized along the nanoscroll axis for these two nanoscrolls, which are 98 and 32 times respectively larger than that of planar monolayer $MoS_2$ in Figure 1b. As shown in eq 4, the second-order susceptibility tensor of single-roll nanoscroll evolves with the rolling angle $\theta_{roll}$ proportionally by $\cos 3\theta_{roll}$, which has a period of 60° if ignoring the sign. The largest SHG tensor element is $\chi^{(2)}_{yyy} = d_0 \cos 3\theta_{roll}$ (ellipticity of cross-section doesn't change $\chi^{(2)}_{yyy}$, see eq 5), which is equal to $-0.83d_0$ and $-0.59d_0$ for nanoscrolls *NS1* and *NS2*. Assuming the nanoscroll has a diameter of $D_{NS}$, and the incident laser beam has a diameter $D_L$ that is larger than $D_{NS}$, then the measured SHG intensity ratio between *N*-roll nanoscroll and monolayer $MoS_2$ can be estimated by,

$$\frac{I_{\mathrm{NS}}}{I_{\mathrm{ML}}} \approx \left(\frac{\pi D_{NS}}{D_L}\frac{N}{2} cos\,(3\theta_{roll})\right)^2 \qquad (6)$$

in which we have assumed the diameter of each scroll increase linearly, $N$ is the roll number, so $\pi N D_{NS}/2$ is the total cross-section length of nanoscroll. In the experiment, the diameter of the

SHG laser beam is about 0.4 μm,[29,30] while the diameter of nanoscrolls is about 0.2 μm according to the optical image and atomic force microscopy (AFM) measurement. Therefore, through the SHG intensity ratio between nanoscrolls and planar monolayer $MoS_2$, the roll numbers of these two nanoscrolls can be estimated to be 13 rolls and 9 rolls respectively according to eq 6. Considering the relatively large diameters and the few rolled layers, the $MoS_2$ nanoscrolls in our experiment are rolled still quite loosely and start with large inner diameters. Molecular dynamics simulations suggest that $MoS_2$ nanoscrolls can be compactly scrolled with a diameter as small as 40 nm (see Supporting Information Section 4), the fabrication of which can greatly enhance the SHG efficiency further.

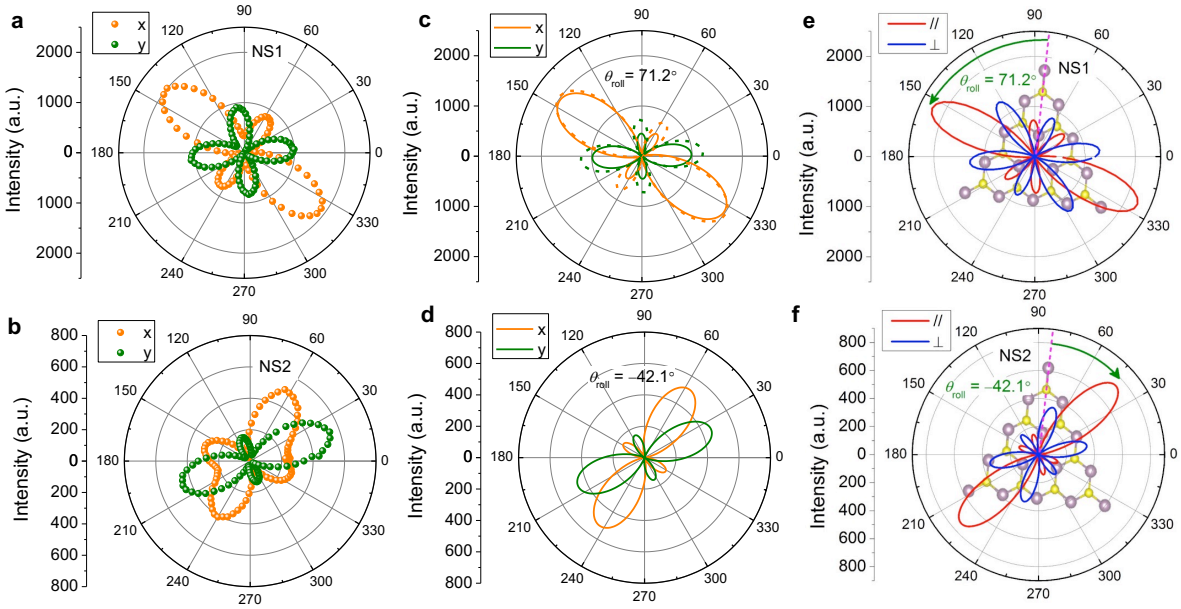


**Figure 4.** (a-b) Experimental polarization-resolved SHG of two $MoS_2$ nanoscrolls with second harmonic field polarized along *x* and *y* directions. (c-d) Calculated SHG pattern for these two nanoscrolls based on their chiralities and the flake triangle rotation angle. The dashed line in (c) is the result considering an elliptical cross-section ($e = 0.15$). (e-f) Calculated SHG with second

harmonic analyzed along parallel and perpendicular directions of incident laser based on the intensity fittings in (c-d) for the same two $MoS_2$ nanoscrolls.

The SHG of nanoscrolls has been well explained by the coherent superposition of SH fields generated by composed $MoS_2$ film. Even though the experiments in this work are conducted for $MoS_2$ nanoscrolls, from the theoretical analysis above, similar chirality-dependent SHG should be expected for $MoS_2$ nanotubes. The chirality of $MoS_2$ nanotube can be defined in Figure 5a. The *(m, n)* index determines the vector $\overrightarrow{C_h} = n \cdot \vec{a} + m \cdot \vec{b}$, which becomes the circumference of $MoS_2$ nanotube after wrapping around the axis $\vec{T}$ as shown in Figure 5b. According to eq 4, the maximum SHG intensity is obtained with both the incident and detected electric field polarized aligned along the nanotube axis. Assuming that the laser beam size is larger than nanotube diameter, the intensity will be proportional to ${A_{NT}}^2 \left|\chi^{(2)}_{yyy}\right|^2 = {A_{NT}}^2 {d_0}^2 \cos^2 3\theta_{roll}$, in which $A_{NT}$ is the outer surface area of the nanotube, $d_0$ is the tensor parameter in eq 1. In comparison, for monolayer $MoS_2$, the maximum SHG intensity will be simply proportional to ${A_{ML}}^2 {d_0}^2$, in which $A_{ML}$ is the area of monolayer $MoS_2$ under the laser beam. Figure 5c plots the SHG intensity of single-walled $MoS_2$ nanotubes with different chiralities, assuming the same nanotube length. The SHG intensity map shows six-fold symmetry, consistent with the hexagonal lattice of monolayer $MoS_2$ and the $\pi$ rotation equivalence of SHG measurement. With a known perimeter of the nanotube, for example, obtained by AFM or scanning electron microscope (SEM) characterization, the chirality of $MoS_2$ nanotube can be non-destructively determined by SHG measurement using SHG intensity of monolayer $MoS_2$ as a reference.

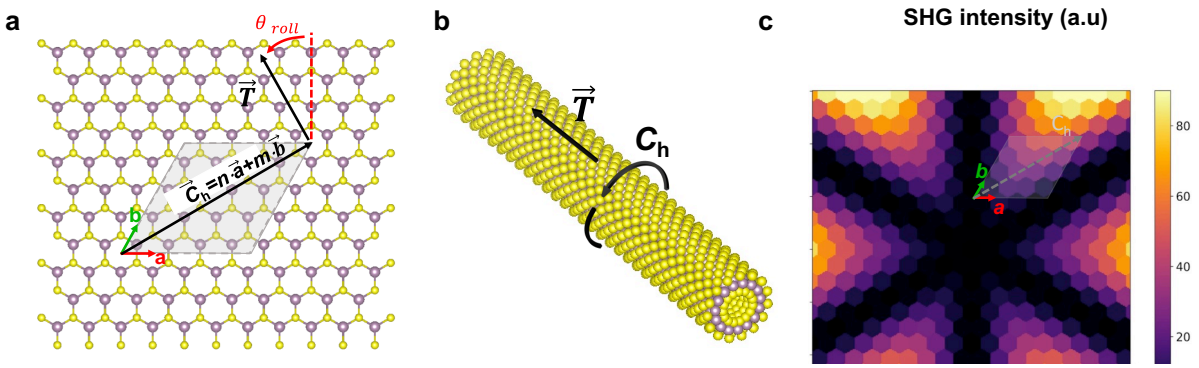


**Figure 5.** (a) Chiral vector definition of $MoS_2$ nanotube $\overrightarrow{C_h} = n \cdot \vec{a} + m \cdot \vec{b}$, in which $\vec{a}$ and $\vec{b}$ are the in-plane primitive lattice vectors of $MoS_2$. (b) Schematic drawing of $MoS_2$ nanotube by wrapping $MoS_2$ sheet along the vector direction $\vec{T}$. (c) SHG intensity map of $MoS_2$ nanotubes with different chiralities.

## CONCLUSIONS

In summary, we have fabricated $MoS_2$ nanoscrolls and characterized their polarization-resolved SHG performance. The polarization-resovled SHG can be well explained by the coherent SH field superposition theory. Both the experimental results and theoretical calculations suggest that the SHG of $MoS_2$ nanoscroll has a strong chirality dependence. Besides $MoS_2$, other non-centrosymmetric 2D materials, such as $WS_2$, $WSe_2$, and hBN,[19,20,24,26,28,31] are expected to show similar chirality-dependent SHG enhancement. In addition, our chirality-dependent SHG characterization can be further explored as a fast, convenient, and non-destructive technique to determine the chiralities of nanoscrolls and nanotubes. Compared with planar monolayer $MoS_2$ or bulk 2H-$MoS_2$, the 1D $MoS_2$ nanoscroll can achieve much higher SHG intensity and thus emission efficiency. In our experiment, a 98-times-stronger SHG intensity has been achieved.

Nevertheless, considering the relatively large diameters (0.2 μm) and the small roll numbers (8-10 rolls) of the nanoscrolls in our experiment, it can be expected that by fabricating more compactly rolled nanoscrolls, even higher SHG efficiency can be achieved. Together with their reduced size and the designable anisotropic nonlinear optical responses, these nanoscrolls can have unique advantages as functional components in integrated photonics such as a microsized frequency converter and optical modulator.[6-8,32]

## METHODS

**Sample preparation.** The monolayer $MoS_2$ flakes were grown by the chemical vapor deposition (CVD) method on $SiO_2$/Si substrate. $MoO_3$ and sulfur powders in two quartz boats were used as solid precursors. The grown $MoS_2$ flakes are of triangular or six-pointed star shape. To form the $MoS_2$ nanoscrolls, 100–500 μL isopropyl alcohol (IPA) was carefully dropped on the substrate. After the solution was vaporized, the $MoS_2$ nanoscrolls were formed.

**SHG measurement.** For the SHG measurements, the sample was excited by a Ti: Sapphire femtosecond laser system (80 fs, 80 MHz, chopped at 1 kHz) centered at 800 nm. The SHG measurement was conducted with a reflection geometry with the excitation laser normal to the sample at room temperature. The generated SHG signal was collected by a modified WITec Alpha 300 S confocal Raman microscope with a 50× objective (NA = 0.75). The pump laser has a spot size of around 400 nm.[29,30] Short-pass dichroic mirror and 400 nm bandpass filter was used to ensure pure SHG signals. The SHG signals were analyzed by a linear polarizer polarized along *x* or *y* direction. To study the SHG polarimetry, the polarization of the incident laser was rotated by a motorized half-wave plate. The laser power was fixed for the SHG polarimetry for both monolayer $MoS_2$ and $MoS_2$ nanoscrolls. The SHG mapping image was taken by scanning the

sample through a piezo-driven stage, with the detected SH polarization fixed at *x* direction and the incident laser polarization tuned to make the monolayer $MoS_2$ intensity largest.

ASSOCIATED CONTENT

**Supporting Information**. The Supporting Information is available free of charge online.

Second-order susceptibility tensor of rotated $MoS_2$ flake and nanoscrolls/nanotubes; the polarization-resolved SHG pattern polarized along *x* and *y* (parallel and perpendicular) directions; molecular dynamics simulations of compactly rolled $MoS_2$ nanoscrolls and the substrate influences.

## AUTHOR INFORMATION

### Corresponding Author

*Email: sjh5899@psu.edu

### Author Contributions

The manuscript was written through contributions of all authors. All authors have given approval to the final version of the manuscript. Q.Q. and R.Z. carried out the SHG measurements. Q.J. and Y.Z. fabricated the $MoS_2$ nanoscroll samples. Q.Q. carried out the data analysis and theoretical calculations of SHG. G.-S.J. conducted the molecular dynamics simulations. Q.Q., K.Z. and S.H. discussed the results. The work was supervised by M.J.B, J.K., V.G. and S.H..

### Notes

The authors declare no competing financial interest.

## ACKNOWLEDGMENT

R. Z. and V.G. acknowledge support from the NSF grant number DMR-1807768 and NSF-MRSEC Penn State Center for Nanoscale Science, grant number DMR- 1420620. Q. J. and J. K. acknowledge the support from the STC Center for Integrated Quantum Materials with NSF grant no. DMR-1231319. G.S.J. acknowledges support by the Laboratory Directed Research and Development (LDRD) Program of Oak Ridge National Laboratory and CADES for computing resources. ORNL is managed by UT-Battelle, LLC, for DOE under contract DE-AC05-00OR22725. G.S.J and M.J.B. acknowledge support by the Office of Naval Research (Grant No. N00014-16-1-233) and DOD-MURI (Grant No. FA9550-15-1-0514).

## REFERENCES

1. Yin, X.; Ye, Z.; Chenet, D. A.; Ye, Y.; O'Brien, K.; Hone, J. C.; Zhang, X. Edge Nonlinear Optics on a $MoS_2$ Atomic Monolayer. *Science* **2014**, 344, 488-490.
2. Song, Y.; Hu, S.; Lin, M.; Gan, X.; Tan, P.; Zhao, J. Extraordinary Second Harmonic Generation in $ReS_2$ Atomic Crystals. *ACS Photonics* **2018**, 5, 3485-3491.
3. Autere, A.; Jussila, H.; Dai, Y.; Wang, Y.; Lipsanen, H.; Sun, Z. Nonlinear Optics with 2D Layered Materials. *Adv. Mater.* **2018**, 30, 1705963.
4. Ribeiro-Soares, J.; Janisch, C.; Liu, Z.; Elias, A. L.; Dresselhaus, M. S.; Terrones, M.; Jorio, L. G. C.; Jorio, A. Second Harmonic Generation in $WSe_2$. *2D Mater.* **2015**, 45015.
5. Kumar, N.; Najmaei, S.; Cui, Q.; Ceballos, F.; Ajayan, P. M.; Lou, J.; Zhao, H. Second harmonic microscopy of monolayer $MoS_2$. *Phy. Rev. B* **2013**, 161403R.
6. Shi, J.; Yu, P.; Liu, F.; He, P.; Wang, R.; Qin, L.; Zhou, J.; Li, X.; Zhou, J.; Sui, X. et al. 3R $MoS_2$ with Broken Inversion Symmetry: A Promising Ultrathin Nonlinear Optical Device. *Adv. Mater.* **2017**, 29, 1701486.
7. Zhao, M.; Ye, Z.; Suzuki, R.; Ye, Y.; Zhu, H.; Xiao, J.; Wang, Y.; Iwasa, Y.; Zhang, X. Atomically phase-matched second-harmonic generation in a 2D crystal. *Light: Sci. Appl.* **2016**, 5, e16131.
8. Yang, D.; Hu, X.; Zhuang, M.; Ding, Y.; Zhou, S.; Li, A.; Yu, Y.; Li, H.; Luo, Z.; Gan, L. et al. Inversion Symmetry Broken 2D 3R-$MoTe_2$. *Adv. Funct. Mater.* **2018**, 28, 1800785.
9. Carletti, L.; Locatelli, A.; Neshev, D.; De Angelis, C. Shaping the Radiation Pattern of Second-Harmonic Generation from AlGaAs Dielectric Nanoantennas. *ACS Photonics* **2016**, 3, 1500-1507.

10. Marino, G.; Gigli, C.; Rocco, D.; Lemaître, A.; Favero, I.; De Angelis, C.; Leo, G. Zero-Order Second Harmonic Generation from AlGaAs-on-Insulator Metasurfaces. *ACS Photonics* **2019**, 6, 1226-1231.
11. Li, Y.; Rao, Y.; Mak, K. F.; You, Y.; Wang, S.; Dean, C. R.; Heinz, T. F. Probing Symmetry Properties of Few-Layer $MoS_2$ and h-BN by Optical Second-Harmonic Generation. *Nano Lett.* **2013**, 13, 3329-3333.
12. Shen, Y. R. Surface properties probed by second-harmonic and sum-frequency generation. *Nature* **1989**, 337, 519-525.
13. Hsu, W.; Zhao, Z.; Li, L.; Chen, C.; Chiu, M.; Chang, P.; Chou, Y.; Chang, W. Second Harmonic Generation from Artificially Stacked Transition Metal Dichalcogenide Twisted Bilayers. *ACS Nano* **2014**, 8, 2951-2958.
14. Jiang, T.; Liu, H.; Huang, D.; Zhang, S.; Li, Y.; Gong, X.; Shen, Y.; Liu, W.; Wu, S. Valley and band structure engineering of folded $MoS_2$ bilayers. *Nat. Nanotechnol.* **2014**, 9, 825-829.
15. Kim, C.; Brown, L.; Graham, M. W.; Hovden, R.; Havener, R. W.; McEuen, P. L.; Muller, D. A.; Park, J. Stacking Order Dependent Second Harmonic Generation and Topological Defects in h-BN Bilayers. *Nano Lett.* **2013**, 13, 5660-5665.
16. Shen, Y. R., *The Principles of Nonlinear Optics*; Wiley: New York, 1984.
17. Malard, L. M.; Alencar, T. V.; Barboza, A. P. M.; Mak, K. F.; de Paula, A. M. Observation of intense second harmonic generation from $MoS_2$ atomic crystals. *Phy. Rev. B* **2013**, 87, 201401R.
18. Mishina, E.; Sherstyuk, N.; Lavrov, S.; Sigov, A.; Mitioglu, A.; Anghel, S.; Kulyuk, L. Observation of two polytypes of $MoS_2$ ultrathin layers studied by second harmonic generation microscopy and photoluminescence. *Appl. Phys. Lett.* **2015**, 106, 131901.
19. Wang, W.; Gai, Y.; Xiao, D.; Zhao, Y. A facile and general approach for production of nanoscrolls with high-yield from two-dimensional nanosheets. *Sci. Rep.* **2018**, 8, 15262.
20. Zhang, C.; Wang, S.; Yang, L.; Liu, Y.; Xu, T.; Ning, Z.; Zak, A.; Zhang, Z.; Tenne, R.; Chen, Q. High-performance photodetectors for visible and near-infrared lights based on individual $WS_2$ nanotubes. *Appl. Phys. Lett.* **2012**, 100, 243101.
21. Deng, W.; You, C.; Chen, X.; Wang, Y.; Li, Y.; Feng, B.; Shi, K.; Chen, Y.; Sun, L.; Zhang, Y. High‐Performance Photodiode Based on Atomically Thin $WSe_2/MoS_2$ Nanoscroll Integration. *Small* **2019**, 15, 1901544.
22. Meng, J.; Wang, G.; Li, X.; Lu, X.; Zhang, J.; Yu, H.; Chen, W.; Du, L.; Liao, M.; Zhao, J. et al. Rolling Up a Monolayer $MoS_2$ Sheet. *Small* **2016**, 12, 3770-3774.
23. Wang, Z.; Wu, H.; Li, Q.; Besenbacher, F.; Zeng, X. C.; Dong, M. Self-scrolling $MoS_2$ metallic wires. *Nanoscale* **2018**, 10, 18178-18185.

24. Hwang, D. Y.; Suh, D. H. Formation of hexagonal boron nitride nanoscrolls induced by inclusion and exclusion of self-assembling molecules in solution process. *Nanoscale* **2014**, 6, 5686-5690.
25. Cui, X.; Kong, Z.; Gao, E.; Huang, D.; Hao, Y.; Shen, H.; Di, C.; Xu, Z.; Zheng, J.; Zhu, D. Rolling up transition metal dichalcogenide nanoscrolls via one drop of ethanol. *Nat. Commun.* **2018**, 9, 1301.
26. Lai, Z.; Chen, Y.; Tan, C.; Zhang, X.; Zhang, H. Self-Assembly of Two-Dimensional Nanosheets into One-Dimensional Nanostructures. *Chem* **2016**, 1, 59-77.
27. van der Zande, A. M.; Huang, P. Y.; Chenet, D. A.; Berkelbach, T. C.; You, Y.; Lee, G.; Heinz, T. F.; Reichman, D. R.; Muller, D. A.; Hone, J. C. Grains and grain boundaries in highly crystalline monolayer molybdenum disulphide. *Nat. Mater.* **2013**, 12, 554-561.
28. Fathipour, S.; Remskar, M.; Varlec, A.; Ajoy, A.; Yan, R.; Vishwanath, S.; Rouvimov, S.; Hwang, W. S.; Xing, H. G.; Jena, D. et al. Synthesized multiwall $MoS_2$ nanotube and nanoribbon field-effect transistors. *Appl. Phys. Lett.* **2015**, 106, 22114.
29. Denev, S. A.; Lummen, T. T. A.; Barnes, E.; Kumar, A.; Gopalan, V. Probing Ferroelectrics Using Optical Second Harmonic Generation. *J. Am. Ceram. Soc.* **2011**, 94, 2699-2727.
30. Lummen, T. T. A.; Gu, Y.; Wang, J.; Lei, S.; Xue, F.; Kumar, A.; Barnes, A. T.; Barnes, E.; Denev, S.; Belianinov, A. et al. Thermotropic phase boundaries in classic ferroelectrics. *Nat. Commun.* **2014**, 5, 3172.
31. Golberg, D.; Bando, Y.; Huang, Y.; Terao, T.; Mitome, M.; Tang, C.; Zhi, C. Boron Nitride Nanotubes and Nanosheets. *ACS Nano* **2010**, 4, 2979-2993.
32. Li, D.; Wei, C.; Song, J.; Huang, X.; Wang, F.; Liu, K.; Xiong, W.; Hong, X.; Cui, B.; Feng, A. et al. Anisotropic Enhancement of Second-Harmonic Generation in Monolayer and Bilayer $MoS_2$ by Integrating with $TiO_2$ Nanowires. *Nano Lett.* **2019**, 19, 4195-4204.

# Supporting Information

## Chirality-Dependent Second Harmonic Generation of $MoS_2$ Nanoscroll with Enhanced Efficiency

*Qingkai Qian,[†] Rui Zu,[‡] Qingqing Ji,[#] Gang Seob Jung,[∥,⊥] Kunyan Zhang,[†] Ye Zhang,[#,§] Markus J. Buehler,[⊥] Jing Kong,[#] Venkatraman Gopalan,[‡,▽] Shengxi Huang*[,†]*

[†]Department of Electrical Engineering, The Pennsylvania State University, University Park, Pennsylvania 16802, United States

[‡]Department of Materials Science and Engineering, The Pennsylvania State University, University Park, Pennsylvania 16802, United States

[#]Department of Electrical Engineering, Massachusetts Institute of Technology, Cambridge, Massachusetts 02139, United States

[∥]Computational Sciences and Engineering Division, Oak Ridge National Laboratory, Oak Ridge, Tennessee 37831, United States

[⊥]Department of Civil and Environmental Engineering, Massachusetts Institute of Technology, Cambridge, Massachusetts 02139, United States

[§]Department of Physics, Mount Holyoke College, South Hadley, Massachusetts 01075, United States

[▽]Department of Physics, and Department of Engineering Science and Mechanics, The Pennsylvania State University, University Park, Pennsylvania 16802, United States

KEYWORDS: $MoS_2$, nanoscroll, nanotube, second harmonic generation, chirality.

## 1. Second-order susceptibility tensor of monolayer $MoS_2$

The second-order susceptibility tensor of monolayer $MoS_2$ after in-plane rotation can be calculated by tensor transformation (See Section 2),

$$\chi^{(2)}_{ijk}(\varphi) = d_0 \begin{pmatrix} \begin{pmatrix} \sin 3\varphi \\ -\cos 3\varphi \\ 0 \end{pmatrix} & \begin{pmatrix} -\cos 3\varphi \\ -\sin 3\varphi \\ 0 \end{pmatrix} & \begin{pmatrix} 0 \\ 0 \\ 0 \end{pmatrix} \\ \begin{pmatrix} -\cos 3\varphi \\ -\sin 3\varphi \\ 0 \end{pmatrix} & \begin{pmatrix} -\sin 3\varphi \\ \cos 3\varphi \\ 0 \end{pmatrix} & \begin{pmatrix} 0 \\ 0 \\ 0 \end{pmatrix} \\ \begin{pmatrix} 0 \\ 0 \\ 0 \end{pmatrix} & \begin{pmatrix} 0 \\ 0 \\ 0 \end{pmatrix} & \begin{pmatrix} 0 \\ 0 \\ 0 \end{pmatrix} \end{pmatrix} \quad \text{(S1)}$$

in which $\varphi$ is defined by counter-clockwise rotation of the $MoS_2$ flake, with $MoS_2$ zigzag direction aligned with *x*-axis as 0°. From this tensor, the SHG intensity measured with parallel and perpendicular directions can be calculated,

$$I_{\parallel} = {d_0}^2 {E_0}^4 \sin^2(3\theta - 3\varphi) \quad \text{(S2)}$$

$$I_{\perp} = {d_0}^2 {E_0}^4 \cos^2(3\theta - 3\varphi) \quad \text{(S3)}$$

in which $\theta$ is polarization direction of the incident electric field. From eq S2 and S3 we can see the rotation $\varphi$ of $MoS_2$ flake will just cause the SHG pattern shift by $\varphi$. If the SHG intensity is measured with *x* and *y* polarizations, the SHG intensity will be,

$$I_x = {d_0}^2 {E_0}^4 \sin^2(2\theta - 3\varphi) \quad \text{(S4)}$$

$$I_y = {d_0}^2 {E_0}^4 \cos^2(2\theta - 3\varphi) \quad \text{(S5)}$$

from which we can see now the rotation $\varphi$ of $MoS_2$ flake will cause $\theta$ of SHG pattern shift by $3\varphi/2$, which is shown in Figure S1.

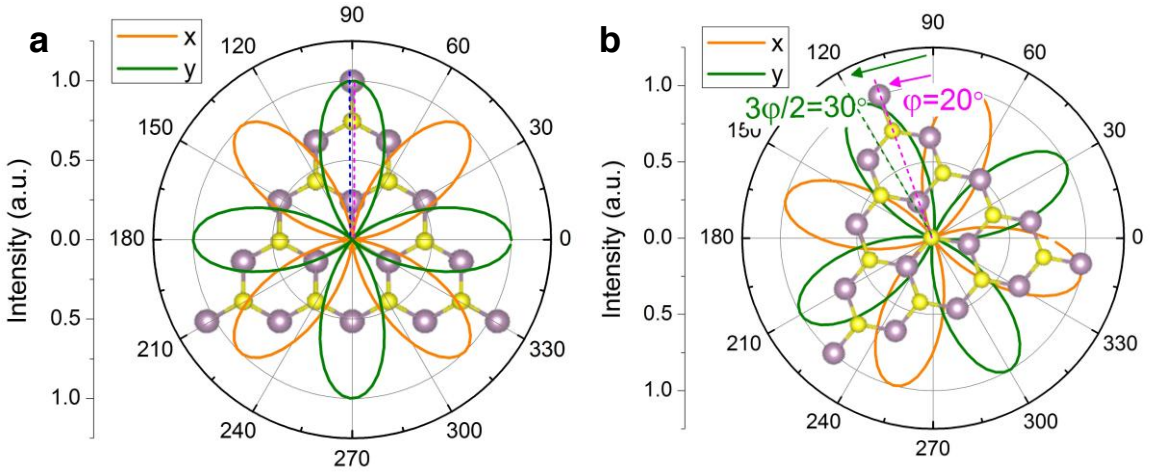


**Figure S1. SHG pattern of rotated $MoS_2$ flake measured with *x* and *y* polarizations.** The rotation of flake by $\varphi$ causes the rotation of SHG pattern by $3\varphi/2$.

## 2. Second-order susceptibility tensor transformation.

The SH field $E_i^{2\omega}$ (or proportionally the generated SH electric dipole) can be calculated by $E_i^{2\omega} = \chi_{ijk}^{(2)} E_j^{\omega} E_k^{\omega}$, according to the definition of second-order susceptibility tensor $\chi_{ijk}^{(2)}$. The rotation matrix $R_{ij}$ rotates the coordinate $r$ of $MoS_2$ flake by $r_i' = R_{ij} r_j$. If the incident electric field $E_j^{\omega}$ is also rotated by $E_i^{\omega\prime} = R_{ij} E_j^{\omega}$, the generated SH field should be $E_i^{2\omega\prime} = R_{ij} E_j^{2\omega}$. Considering $R^{-1}{}_{ij} R_{jk} = \delta_{ik}$, we can derive,

$$E_l^{2\omega\prime} = (R_{li} \chi_{ijk}^{(2)} R^{-1}{}_{jo} R^{-1}{}_{kp}) E_o^{\omega\prime} E_p^{\omega\prime} \qquad \text{(S6)}$$

in which $E_o^{\omega\prime}$ and $E_l^{2\omega\prime}$ are electric field in the same coordinates after the material is rotated by $R_{ij}$. All the indexes run for *x*, *y*, *z*, and the Einstein summation notation is used. From eq S6, we can get the second-order susceptibility tensor after material rotation in the same coordinates,

$$\chi_{lop}^{(2)\prime} = R_{li}\chi_{ijk}^{(2)}{R^{-1}}_{jo}{R^{-1}}_{kp} \qquad \text{(S7)}$$

### 3. SHG pattern of rotated 1D $MoS_2$ nanoscroll.

As described in the main text, the second-order susceptibility tensor normalized by its area of 1D $MoS_2$ nanoscroll with its axis in *y* direction is,

$$\chi_{ijk}^{(2)}(\text{nanoscroll}) = d_0 \begin{pmatrix} \begin{pmatrix} 0 \\ -0.5\cos 3\theta_{roll} \\ 0 \end{pmatrix} & \begin{pmatrix} -0.5\cos 3\theta_{roll} \\ 0 \\ 0 \end{pmatrix} & \begin{pmatrix} 0 \\ 0 \\ 0 \end{pmatrix} \\ \begin{pmatrix} -0.5\cos 3\theta_{roll} \\ 0 \\ 0 \end{pmatrix} & \begin{pmatrix} 0 \\ \cos 3\theta_{roll} \\ 0 \end{pmatrix} & \begin{pmatrix} 0 \\ 0 \\ -0.5\cos 3\theta_{roll} \end{pmatrix} \\ \begin{pmatrix} 0 \\ 0 \\ 0 \end{pmatrix} & \begin{pmatrix} 0 \\ 0 \\ -0.5\cos 3\theta_{roll} \end{pmatrix} & \begin{pmatrix} 0 \\ -0.5\cos 3\theta_{roll} \\ 0 \end{pmatrix} \end{pmatrix} \qquad \text{(S8)}$$

in which $\theta_{roll}$ defines the rolling direction and chirality of nanoscroll. If the nanoscroll is rotated counter-clockwise by $\phi$ with rotation matrix $R$, then the rotated tensor can be calcualted by tensor transformation $\chi_{ijk}^{(2)}(nanoscroll, \phi) = R_{im}\,\chi_{mnp}^{(2)}\,{R^{-1}}_{nj}\,{R^{-1}}_{pk}$, resulting in,

$$\chi_{ijk}^{(2)}(\text{nanoscroll}, \phi) = d_0 \begin{pmatrix} \begin{pmatrix} \frac{1}{4}\cos 3\theta_{roll}\sin\phi\,(1+5\cos 2\phi) \\ \frac{1}{4}\cos 3\theta_{roll}\cos\phi\,(3-5\cos 2\phi) \\ 0 \end{pmatrix} & \begin{pmatrix} \frac{1}{4}\cos 3\theta_{roll}\cos\phi\,(3-5\cos 2\phi) \\ -\frac{1}{4}\cos 3\theta_{roll}\sin\phi\,(3+5\cos 2\phi) \\ 0 \end{pmatrix} & \begin{pmatrix} 0 \\ 0 \\ \frac{1}{2}\cos 3\theta_{roll}\sin\phi \end{pmatrix} \\ \begin{pmatrix} \frac{1}{4}\cos 3\theta_{roll}\cos\phi\,(3-5\cos 2\phi) \\ -\frac{1}{4}\cos 3\theta_{roll}\sin\phi\,(3+5\cos 2\phi) \\ 0 \end{pmatrix} & \begin{pmatrix} -\frac{1}{4}\cos 3\theta_{roll}\sin\phi\,(3+5\cos 2\phi) \\ \frac{1}{4}\cos 3\theta_{roll}\cos\phi\,(-1+5\cos 2\phi) \\ 0 \end{pmatrix} & \begin{pmatrix} 0 \\ 0 \\ -\frac{1}{2}\cos 3\theta_{roll}\cos\phi \end{pmatrix} \\ \begin{pmatrix} 0 \\ 0 \\ \frac{1}{2}\cos 3\theta_{roll}\sin\phi \end{pmatrix} & \begin{pmatrix} 0 \\ 0 \\ -\frac{1}{2}\cos 3\theta_{roll}\cos\phi \end{pmatrix} & \begin{pmatrix} \frac{1}{2}\cos 3\theta_{roll}\sin\phi \\ -\frac{1}{2}\cos 3\theta_{roll}\cos\phi \\ 0 \end{pmatrix} \end{pmatrix} \qquad \text{(S9)}$$

For nanoscrolls in the main text with triangle flake rotation $\varphi$, we just need to replace $\phi$ by $\phi = \theta_{roll} + \varphi$. From this tensor in eq S9, the SHG intensity of 1D nanoscroll measured with parallel and perpendicular polarizations can be calculated,

$$I_{\parallel} = \frac{1}{64}{E_0}^4\cos^2 3\theta_{roll}\left\{-5\sin(3\theta - 3\phi) + 3\sin(\theta - \phi)\right\}^2 \qquad \text{(S10)}$$

$$I_{\perp} = \frac{1}{64} E_0{}^4 \cos^2 3\theta_{roll} \{-5\cos(3\theta - 3\phi) + 3\cos(\theta - \phi)\}^2 \qquad \text{(S11)}$$

from which we also can see the rotation $\varphi$ of nanoscroll will only cause $\theta$ of SHG pattern shift by $\varphi$. If the SHG intensity is measured with *x* and *y* polarizations, the SHG intensity will be,

$$I_x = \frac{1}{64} E_0{}^4 \cos^2 3\theta_{roll} \{-5\sin(2\theta - 3\phi) + \sin(2\theta - \phi) - 2\sin\phi\}^2 \qquad \text{(S12)}$$

$$I_y = \frac{1}{64} E_0{}^4 \cos^2 3\theta_{roll} \{5\cos(2\theta - 3\phi) + \cos(2\theta - \phi) - 2\cos\phi\}^2 \qquad \text{(S13)}$$

The rotation of nanoscroll will change the SHG pattern measured with *x* and *y* polarizations in a complex way, as plotted in Figure S2.

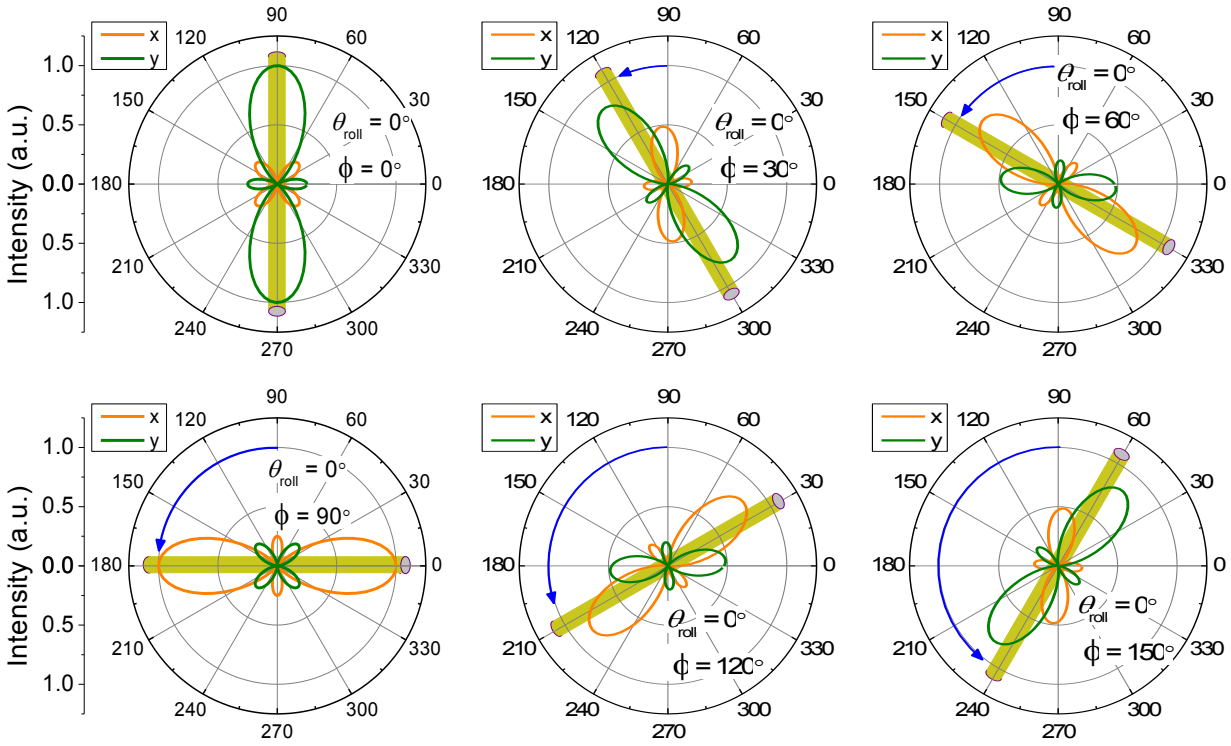


**Figure S2. SHG pattern of rotated 1D $MoS_2$ flake measured with *x* and *y* polarizations.** The chirality of nanoscroll is fixed ($\theta_{roll} = 0°$).

## 4. Compactly rolled $MoS_2$ nanoscrolls and the substrate influences.

In our experiment, the $MoS_2$ nanoscrolls have relatively large diameters (~200 nm) but few roll layers (9 to 13 layers). The formation of more compactly rolled $MoS_2$ nanoscrolls can greatly enhance the SHG efficiency further. Molecular dynamics (MD) simulations are conducted to verify the physical viability and the possible limits of forming more compactly rolled $MoS_2$ nanoscrolls. MD simulations are performed *via* the LAMMPS package.[1] Reactive Empirical Bond Order (REBO) force field (FF)[2,3] is utilized for the interatomic interactions of $MoS_2$. The original REBO parameters have been further tuned based on the Density Functional Theory (DFT) calculations,[4,5] which can better describe the binding energy and the interlayer distance of the stacking geometries.

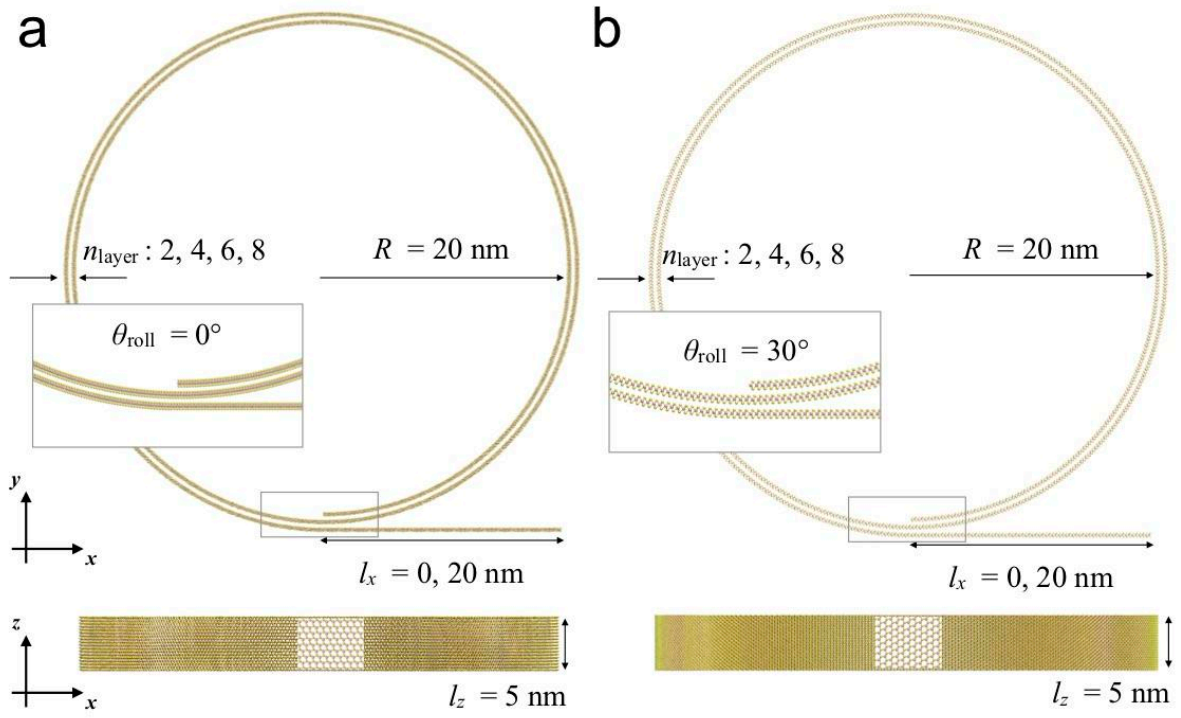


**Figure S3. Initial geometries of $MoS_2$ nanoscroll for molecular dynamics simulation.** Two different rolling directions ($\theta_{roll}$ = 0 and 30°) are considered. Each rolling direction has four

different numbers of layers ($n_{layer}$) varied from 2 to 8 with/without considering the substrate effects. The structural relaxations are performed through MD runs for a total of 16 models. The substrate effects through Lennard-Jones wall are turned on/off and investigated by controlling $l_x$ (0 or 20 nm).

The initial rolled-up atomistic models are shown in Figure S3. The initial scroll geometries are estimated by

$$r(\theta) = R + \frac{h}{2\pi}\theta, \qquad \text{(S14)}$$

where $h$ is the interlayer distance between layers set as 6.7 Å, which is the equilibrium distance of the AA stacking; $R$ is the radius of the inner circle; $\theta$ is the rotation angle starting from the negative y-axis. The total length of the monolayer $MoS_2$ in $n_{layer}$ nanoscroll is calculated by

$$l_{total} = 2\pi R n_{layer} + \pi h n_{layer}^2 \qquad \text{(S15)}$$

The samples in our experiments have a substantial area of $MoS_2$ that is still flat on a substrate, which is used to identify the lattice orientations and rolling directions. MD simulations with similar flat $MoS_2$ region on substrate is conducted to see the effects of the existing substrate and the non-scrolled $MoS_2$ monolayers. The vdW interaction with the substrate is modeled through Lennard-Jones (LJ) potential with 9-3 form of

$$E = \varepsilon[\frac{2}{15}\left(\frac{\sigma}{r}\right)^9 - (\frac{\sigma}{r})^3] \qquad \text{(S16)}$$

where $r$ is the distance between atom and substrate; $\sigma$ and $\varepsilon$ are the parameters related to the equilibrium distance and adhesion energy. We choose the same values used in the previous study

for the $MoS_2$ channel growth as $\sigma$ = 2.3 Å and $\varepsilon$ = 0.1 eV.[6] We note that we only consider the LJ interaction to see whether there are any differences due to the substrate interaction. We apply the structure relaxation for each model with the NPT ensemble at 300 K and 0 bar up to 500 ps after the energy minimization.

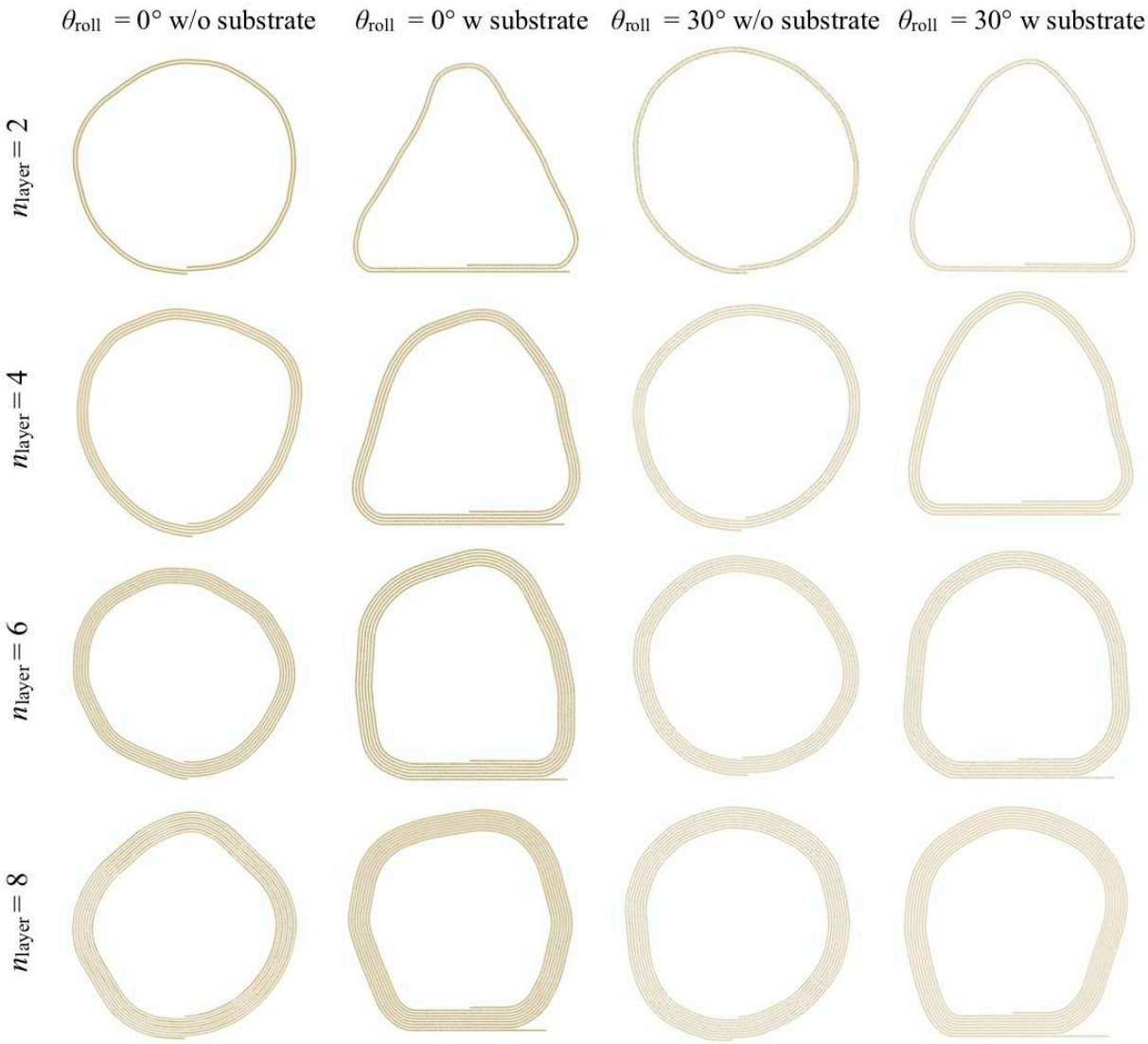


**Figure S4. Snap-shots of nanoscroll geometries after molecular dynamics relaxations.** Cross-sections of the nanoscrolls with two different rolling directions ($\theta_{roll}$ = 0 and 30°) and four different layer numbers with and without the LJ substrates.

Figure S4 shows the relaxed nanoscroll cross-section. Our calculations suggest that $MoS_2$ nanoscroll can be compactly rolled with much smaller diameter (40 nm at least in these simulations). A previous study also reported that the diameters of nanoscroll can be as small as 10-40 nm.[7] Once $MoS_2$ forms a scroll, the main driving force for the further rolling is the vdW interaction.[8] The stability of the nanoscroll comes from the balance between the vdW interaction and the bending energy. Also, the high friction force from stacking geometries can contribute to the stability with the various radius.[5] If there is a non-scrolled flat region interacting with the substrate, the shape is distorted from the circle, supporting our elliptical cross-section assumption in Figure 3a ($e > 0$).

**5. SHG pattern of 1D $MoS_2$ nanoscroll with elliptical cross-section.**

For nanoscroll with elliptical cross section, with the ellipticity defined by $e = (a-b)/(a+b)$ as shown in Figure S6, the second-order susceptibility tensor of single-walled nanoscroll normalized by its film area with nanoscroll axis in *y* direction can be numerically calculated by,

$$\chi_{ijk}^{(2)}(\text{elliptic nanoscroll}) = \int_0^{2\pi} \chi_{ijk}^{(2)}\left(R_{\theta_{roll},\varphi_{roll}}\right) L(e,\varphi_{roll}) d\varphi_{roll} \,/\, \int_0^{2\pi} L(e,\varphi_{roll}) d\varphi_{roll} \qquad \text{(S17)}$$

in which $R_{\theta_{roll},\varphi_{roll}}$ is the rotation matrix of $MoS_2$ film to a part of nanoscroll/nanotube walls by roll angle $\varphi_{roll}$ around the nanoscroll axis. $\chi_{ijk}^{(2)}\left(R_{\theta_{roll},\varphi_{roll}}\right)$ is the second-order susceptibility tensor after rotation $R_{\theta_{roll},\varphi_{roll}}$ according to eq S7. $L(e,\varphi_{roll})d\varphi_{roll}$ is the perimeter increase of nanoscroll cross section caused by $d\varphi_{roll}$, which is not the same for different $\varphi_{roll}$ value and serves as a weight for the tensor calculation. There is no analytic form for the perimeter of ellipse $\int_0^{2\pi} L(e,\varphi_{roll})d\varphi_{roll}$. The tensor can be numerically calculated and well approximated by the following analytical equation with all tensor element errors in the parentheses smaller than 0.014

as plotted in Figure S5, which are ignorable compared with the largest element 1 in the parentheses.

$$\chi_{ijk}^{(2)}(\text{elliptical nanoscroll}) \approx d_0 \cos 3\theta_{roll} \begin{pmatrix} \begin{pmatrix} 0 \\ -0.5-0.5\sin\left(\frac{e\pi}{2}\right) \\ 0 \end{pmatrix} & \begin{pmatrix} -0.5-0.5\sin\left(\frac{e\pi}{2}\right) \\ 0 \\ 0 \end{pmatrix} & \begin{pmatrix} 0 \\ 0 \\ 0 \end{pmatrix} \\ \begin{pmatrix} -0.5-0.5\sin\left(\frac{e\pi}{2}\right) \\ 0 \\ 0 \end{pmatrix} & \begin{pmatrix} 0 \\ 1 \\ 0 \end{pmatrix} & \begin{pmatrix} 0 \\ 0 \\ -0.5+0.5\sin\left(\frac{e\pi}{2}\right) \end{pmatrix} \\ \begin{pmatrix} 0 \\ 0 \\ 0 \end{pmatrix} & \begin{pmatrix} 0 \\ 0 \\ -0.5+0.5\sin\left(\frac{e\pi}{2}\right) \end{pmatrix} & \begin{pmatrix} 0 \\ -0.5+0.5\sin\left(\frac{e\pi}{2}\right) \\ 0 \end{pmatrix} \end{pmatrix} \quad \text{(S18)}$$

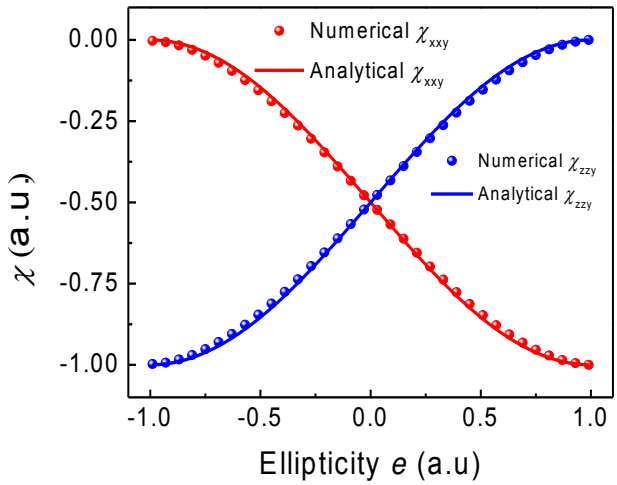


**Figure S5. Second-order susceptibility tensor elements of nanoscroll with elliptical cross-section as a function of ellipticity *e*.** The dots are numerical results, while the solid lines are analytical results from eq S18.

Figure S6 numerically calculates the polarization-resolved SHG patterns of nanoscrolls/nanotubes with an elliptical cross-section based on eq S18. All these nanoscrolls are rolled with $\theta_{roll} = 0°$ and have the same perimeter. For nanoscroll with oblate cross-section ($e = 0.3$ in Figure S6a), because its sidewall has less contribution, the SHG intensity is stronger than those with circular ($e = 0$) and prolate ($e < 0$) cross-sections, when the incident laser is not polarized along the nanoscroll axis. This trend can be more easily understood from eq S18 by the

extreme case when $e = 1$ or $e = -1$, which just becomes a tensor of horizontally or vertically oriented $MoS_2$ bilayers. This numerical analysis also further validates our vertical sidewall explanation of the decreased ratio between $\chi^{(2)}_{xxy}$, $\chi^{(2)}_{xyx}$, $\chi^{(2)}_{yxx}$ and $\chi^{(2)}_{yyy}$ for nanoscrolls.

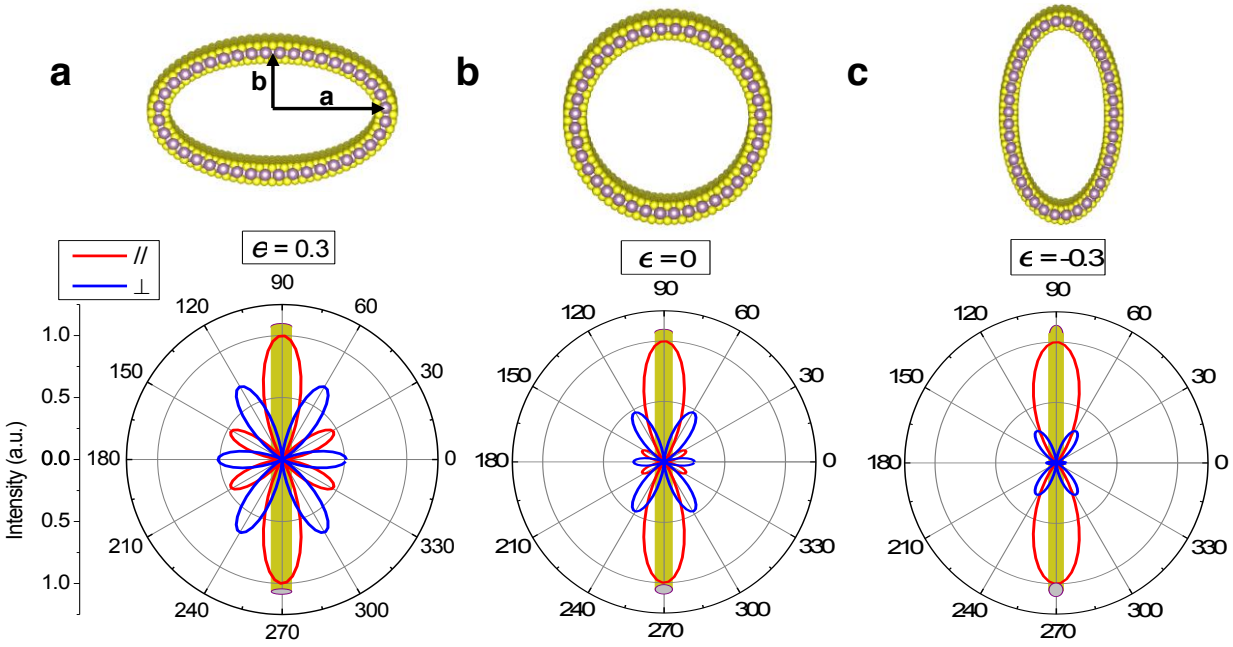


**Figure S6.** (a-c) Calculated polarization resolved SHG of $MoS_2$ nanoscrolls/nanotubes with different elliptical cross-sections. The nanoscrolls/nanotubes are rolled with $\theta_{roll} = 0°$. Ellipticity of the cross-section is defined by $e = (a - b)/(a + b)$. Nanotube with positive ellipticity in (a) has large side petals compared with nanotubes in (b) and (c), due to its smaller area of vertical sidewalls.

### 6. *x*- and *y*-polarized SHG pattern with mirror-symmetry.

If the SHG can be described by a second-order susceptibility tensor $\chi$, the *x*- and *y*-polarized SHG patterns can be calculated by,

$$I_x = {E_0}^4(\frac{\chi_{xxx}+\chi_{xyy}}{2} + \chi_{xxy} \cdot sin2\theta + \frac{\chi_{xxx}-\chi_{xyy}}{2} \cdot cos2\theta)^2 \quad \text{(S19)}$$

$$I_y = {E_0}^4(\frac{\chi_{yyy}+\chi_{xxy}}{2} + \chi_{xyy} \cdot sin2\theta + \frac{\chi_{xxy}-\chi_{yyy}}{2} \cdot cos2\theta)^2 \quad \text{(S20)}$$

We know $A \cdot sin2\theta + \mathrm{B} \cdot cos2\theta$ can always be written as $\mathrm{C} \cdot \sin(2\theta + \theta_0)$, in which $\mathrm{C} = \sqrt{A^2 + B^2}$, $\theta_0 = \arctan(B/A)$, so polar plot of $\mathrm{C} \cdot \sin(2\theta + \theta_0)$ will be symmetric with respect to the axes $\theta = \frac{\pi}{4} - \frac{\theta_0}{2}$ or $\theta = \frac{3\pi}{4} - \frac{\theta_0}{2}$ (when $2\theta + \theta_0 = \frac{\pi}{2}$ or $\frac{3\pi}{2}$). As a result, from eq S19 and S20, the SHG pattern explained by one second-order susceptibility tensor $\chi$ will always have mirror symmetry.

**REFERENCES**


1. Plimpton, S. J. Fast Parallel Algorithms for Short-Range Molecular Dynamics. *J*. *Comput*. *Phys*. **1995**, *117*, 1-19.
2. Stewart, J. A.; Spearot, D. E. Atomistic Simulations of Nanoindentation on the Basal Plane of Crystalline Molybdenum Disulfide ($MoS_2$). *Modell*. *Simul*. *Mater*. *Sci*. *Eng*. **2013**, *21*, 45003.
3. Liang, T.; Phillpot, S. R.; Sinnott, S. B. Parametrization of a Reactive Many-Body Potential for Mo-S Systems. *Phy*. *Rev*. *B* **2009**, *79*, 245110.
4. Wang, S.; Qin, Z.; Jung, G. S.; Martin-Martinez, F. J.; Zhang, K.; Buehler, M. J.; Warner, J. H. Atomically Sharp Crack Tips in Monolayer $MoS_2$ and Their Enhanced Toughness by Vacancy Defects. *ACS Nano* **2016**, *10*, 9831-9839.
5. Jung, G. S.; Wang, S.; Qin, Z.; Martin-Martinez, F. J.; Warner, J. H.; Buehler, M. J. Interlocking Friction Governs the Mechanical Fracture of Bilayer $MoS_2$. *ACS Nano* **2018**, *12*, 3600-3608.
6. Han, Y.; Li, M.; Jung, G.; Marsalis, M. A.; Qin, Z.; Buehler, M. J.; Li, L.; Muller, D. A. Sub-Nanometre Channels Embedded in Two-Dimensional Materials. *Nat*. *Mater*. **2018**, *17*, 129-133.
7. Cui, X.; Kong, Z.; Gao, E.; Huang, D.; Hao, Y.; Shen, H.; Di, C.; Xu, Z.; Zheng, J.; Zhu, D. Rolling Up Transition Metal Dichalcogenide Nanoscrolls *via* One Drop of Ethanol. *Nat*. *Commun*. **2018**, *9*, 1301.
8. Wang, Z.; Wu, H.; Li, Q.; Besenbacher, F.; Zeng, X. C.; Dong, M. Self-Scrolling $MoS_2$ Metallic Wires. *Nanoscale* **2018**, *10*, 18178-18185.